Lawrence Berkeley National Laboratory
LBL Publications

Title
Mechanical properties, failure mechanisms, and scaling laws of bicontinuous nanoporous metallic glasses

Permalink
https://escholarship.org/uc/item/2rt1h2ft

Authors
Liu, Chang
Yuan, Suyue
Im, Jinwoo
et al.

Publication Date
2022-10-01

DOI
10.1016/j.actamat.2022.118255

Copyright Information
This work is made available under the terms of a Creative Commons Attribution-NonCommercial License, available at https://creativecommons.org/licenses/by-nc/4.0/

Peer reviewed

eScholarship.org Powered by the California Digital Library
University of California

Acta Materialia 239 (2022) 118255

Contents lists available at ScienceDirect

Acta Materialia

journal homepage: www.elsevier.com/locate/actamat

Full length article

Mechanical properties, failure mechanisms, and scaling laws of bicontinuous nanoporous metallic glasses

Chang Liu[a], Suyue Yuan[a], Jinwoo Im[b], Felipe P.J. de Barros[b], Sami F. Masri[b,c], Paulo S. Branicio[a,*]

[a] Mork Family Department of Chemical Engineering and Materials Science, University of Southern California, Los Angeles, CA 90089, United States
[b] Sonny Astani Department of Civil and Environmental Engineering, University of Southern California, Los Angeles, CA 90089, United States
[c] Aerospace and Mechanical Engineering, University of Southern California, Los Angeles, CA 90089, United States

ARTICLE INFO

Article history:
Received 24 May 2022
Revised 11 July 2022
Accepted 6 August 2022
Available online 17 August 2022

Keywords:
Nanoporous metallic glass
Mechanical behavior
Scaling laws
Bicontinuous nanoporous

ABSTRACT

Molecular dynamics simulations are employed to study the mechanical properties of nanoporous Cu_xZr_{1-x} metallic glasses (MGs) with five different compositions, $x = 0.28$, 0.36, 0.50, 0.64, and 0.72, and porosity in the range $0.1 < \phi < 0.7$. Results from tensile loading simulations indicate a strong dependence of Young's modulus, E, and Ultimate Tensile Strength (UTS) on porosity and composition. By increasing the porosity from $\phi = 0.1$ to $\phi = 0.7$, the topology of the nanoporous MG shifts from closed cell to open-cell bicontinuous. The change in nanoporous topology enables a brittle-to-ductile transition in deformation and failure mechanisms from a single critical shear band to necking and rupture of ligaments. Genetic Programming (GP) is employed to find scaling laws for E and UTS as a function of porosity and composition. A comparison of the GP-derived scaling laws against existing relationships shows that the GP method is able to uncover expressions that can predict accurately both the values of E and UTS in the whole range of porosity and compositions considered.

© 2022 Acta Materialia Inc. Published by Elsevier Ltd. All rights reserved.

1. Introduction

Benefiting from a disordered atomic arrangement, metallic glasses (MGs) have many unique properties, such as high hardness, strength, and wear resistance [1–3]. By introducing pores in their structure, porous MGs (PMGs) synergize the qualities of porous structures and MGs. That enables strong and lightweight materials, which are suitable for various structural and functional applications, such as catalysis [4,5], sensing [6], dye degradation [7], membrane filters [8], and gas absorption [9]. PMGs can be obtained by various methods such as water vapor release [10], salt dissolution [11], and low-pressure infiltration of hollow carbon microspheres [12]. Some possible applications of PMGs benefit from a high surface to volume ratio, i.e., high specific area. PMGs with pore size in the nanometer scale maximize the specific area and are gaining more and more interest from the community. Tanaka et al. [13] fabricated Pd-based nanoporous MGs (NPMGs) by chemical dealloying a $Pd_{30}Ni_{50}P_{20}$ MG. The 30–60 nm sized nanopores were shown to enhance remarkably the catalytic activity and reusability. Jiao et al. [14] fabricated 3-dimensional bicontinuous NPMGs by selectively dealloying of spinodally decomposed MG precursors and passivation. The underlying dealloying process can be adjusted for tuning the pore size in such nanoporous structures. The stochastic nature of the spinodal decomposition process and the nano-length scale of the porous features result in a high specific surface area making such material a promising candidate for gas absorption.

While MGs have attracted considerable interest due to their mechanical properties, their significant brittleness, which can lead to catastrophic failure, notably limits their possible applications. Surprisingly, recent studies of the mechanical properties of NPMGs have suggested that the introduction of pores and nanopores is able to alleviate the brittleness inherent to MGs. Atomistic investigations, e.g., using molecular dynamics (MD) simulations, have been increasingly used to complement experiments and unveil the underlying deformation mechanisms of NPMG during tensile loading [15–19]. Sopu et al. [15] employed MD to study $Cu_{64}Zr_{36}$ NPMGs and concluded that a structure with nanopores with optimized size and distribution could achieve homogenous plastic deformation while maintaining the strength close to that of monolithic bulk MGs (BMGs). Liu et al. [16] investigated the mechanical behavior of Ta NPMGs and found that the spatial distribution of pores and pore sizes have a strong influence on the displayed ductility. Lin et al. [17] simulated the tensile loading mechanical response of $Cu_{50}Zr_{50}$ NPMGs with well-defined cylindrical ligaments

* Corresponding author.
E-mail address: branicio@usc.edu (P.S. Branicio).

https://doi.org/10.1016/j.actamat.2022.118255
1359-6454/© 2022 Acta Materialia Inc. Published by Elsevier Ltd. All rights reserved.

and observed a slenderness ratio dependent failure by necking. Liu et al. [18] investigated the tensile loading behavior of stochastic $Cu_{64}Zr_{36}$ bicontinuous NPMGs showing an anomalous ductile behavior, displaying an extended plastic regime and a gracious failure by collective ligaments necking. They described the deformation mechanism as a synergistic combination of delocalized necking of ligaments mostly aligned with the loading direction and concurrent progressive reorientation of remaining ligaments. In a similar study, Zhang et al. [19] investigated the sensitivity of the mechanical properties of $Cu_{50}Zr_{50}$ bicontinuous NPMG to porosity and temperature. They also attributed the plasticity found to the bending of the ligaments. Experimentally, it is challenging to directly apply tensile loading simulations on nanoporous samples. Instead, nanoindentation experiments are often conducted to evaluate the tensile behavior of nanoporous samples. Zhang et al. [20] employed nanoindentation, tension, and compression loading to evaluate the deformation behavior of $Cu_{55.4}Zr_{35.2}Al_{7.5}Y_{1.9}$ NPMG prepared using selective dissolution and found bending of ligaments and collapse of ligament nodes in the early stage of deformation, followed by plastic deformation and failure of ligaments.

While monolithic MGs have well defined mechanical properties, those of NPMGs depend on their porous structure topology. Efforts have been spent in developing scaling laws for NPMGs based on experimental results and theoretical calculations [19–26]. However, current scaling laws are developed empirically or based on simplified topology models that consider only porosity as a variable. Functional relationships depending on multiple variables, such as porosity and composition, can be developed using Artificial Intelligence (AI) based methods. The emergence of AI methods is bringing a new dawn to the development of materials science [27,28]. Machine Learning (ML) and Genetic Programming (GP) algorithms have been experiencing resurgence in recent years within the materials science community [29,30]. AI technologies can provide researchers with tools to overcome the barriers between designing, synthesizing, and processing materials by accelerating simulations [31,32], prediction of properties [26,33–36], design of synthetic routes [37,38], optimization of experimental parameters [39,40], and enhancement of characterization methods [41,42]. As for nanoporous materials, it is challenging to predict the mechanical properties due to their complex geometry. A suitable AI method, such as GP, which mimics natural selection, can be employed to describe the functional relationship between bicontinuous NPMGs mechanical properties and system variables.

Motivated by Darwin's theory of natural selection, GP is a powerful evolutionary technique commonly used to automatically generate programs suitable for user-defined tasks [43]. AI technologies are currently enabling the uncovering of physical laws. Among the AI methods, GP is a promising technique to acomplish symbolic regression, allowing one to find suitable mathematical models describing data, when little knowledge of the data structure or distribution is available [44,45]. Within the GP-based symbolic regression (GPSR), expressions are randomly generated and evolve in successive generations, which improve the description of the relationships of interest [46]. GPSR has already been applied to numerous problems [47]. In contrast to other AI methods [48–50], one can derive physical insights from the expressions obtained with the GP method. Chopra et al. [51] developed GP models to predict the compressive strength of concrete based on in situ data from literature. Cai et al. [52] used GPSR to derived heat transfer correlations, including the equation functional and its parameters, from experimental data on heat transfer measurements, which were used to predict the performance of thermal components. Langdon and Barrett [52] applied GP in drug discovery by evolving simple, biologically interpretable, *in silico* models of human oral bioavailability. Barmpalexis et al. [52] found a function mapping levels of four polymers to three different properties of a pharmaceutical release tablet with help of GPSR. Recently, Im et al. [53] applied the GP methodology to identify governing equations in non-linear multiphysics systems.

Table 1
Thermal and mechanical properties of BMG samples with different composition. Glass transition temperature (T_g), molar volume ($\bar{V}$), Young's modulus (E), and ultimate tensile strength (UTS) values are shown with appropriate units.

	T_g (K)	$\bar{V}$ (cm^3/mol)	E (GPa)	UTS (GPa)
$Cu_{25}Zr_{75}$	644	12.25	50.5488	1.84
$Cu_{36}Zr_{64}$	650	11.47	54.5683	2.13
$Cu_{50}Zr_{50}$	664	10.49	59.6166	2.42
$Cu_{64}Zr_{36}$	686	9.52	69.5546	3.31
$Cu_{72}Zr_{28}$	699	9.049	71.8196	3.26

In the present work, we use MD simulations to study the mechanical properties of CuZr bicontinuous NPMGs. We then apply GPSR to derive scaling laws describing the mechanical behavior as a function of system variables and compare them against existing scaling relationships. The results indicate that the GPSR-derived models are able to predict accurately both the Young's modulus, E, and ultimate tensile strength (UTS) as a function of relative density and alloy composition. This research demonstrates that the GPSR is able to uncover expressions that can predict accurately the mechanical properties and also provide physical insights into complex systems.

2. Methods

2.1. Model generation and morphology characterization

Initially, cubic CuZr BMG simulation cells with 5.4 nm sides are prepared following the same procedure as reported previously [54]. Five different compositions, 0.25, 0.36, 0.50, 0.64, and 0.72 Cu are selected to study the effect of compositions on the mechanical behavior of bicontinuous NPMG. We chose this composition range because it is reported that the experimental CuZr BMGs can be synthesized within this range [55]. Periodic boundary conditions are applied along the three cartesian directions. The small BMG cubic system is then replicated multiple times along the *x*, *y*, and *z* directions to obtain large BMG samples. To study the effect of ligament size (ligament diameter) while controlling the porosity, we create $Cu_{64}Zr_{36}$ BMG samples with different side lengths varying from 43.2 nm to 81.0 nm. For all the other compositions, we use a sample side length of 54 nm. The large systems containing 512 - 3,375 small cubes are then relaxed at 800 K for 0.25 ns to minimize periodic patterns in the sample. The final BMG models are obtained after subsequent quenching to 50 K using a -15 K/ps cooling rate. The glass transition temperature, T_g, molar volume, $\bar{V}$, as well as the values of E and UTS of the BMG samples with different concentrations are shown in Table 1.

To generate a bicontinuous nanoporous structure based on the BMG sample, we use the level set method reported previously by Liu and Branicio [56]. Different level sets are then applied to generate samples with various relative densities. In order to ensure the same morphology for all the samples with different side lengths, we keep the product of the wavenumber q_0 and the side length L constant:

$$q_0 L = C_o, \tag{1}$$

where C_o denotes a constant. The morphologies of the samples with different porosities are shown in Fig. 1(a).

Taking three 2-nm slices at random positions along each direction, we employ the AQUAMI package [57] to evaluate the average ligament size, based on measures of the ligament diameter, and ligament size distribution for samples with side length of 54

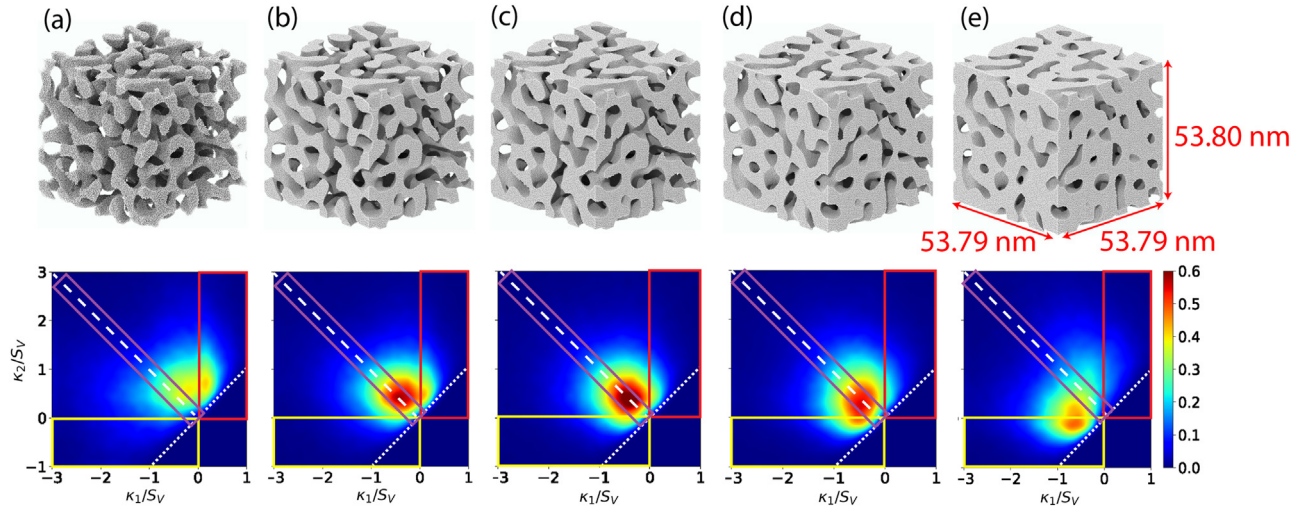

Fig. 1. Initial bicontinuous nanoporous metallic glass (BNPMG) structures for samples with relative density ρ = 0.3, 0.4, 0.5, 0.6, and 0.7 and corresponding curvature distributions. Colors in the lower plots indicate principal curvature probability density. Yellow, red, and purple boxes indicate regions with concave, convex, and saddle surfaces. Dashed lines indicate opposite values of the principal curvatures while the dotted lines indicate identical values.

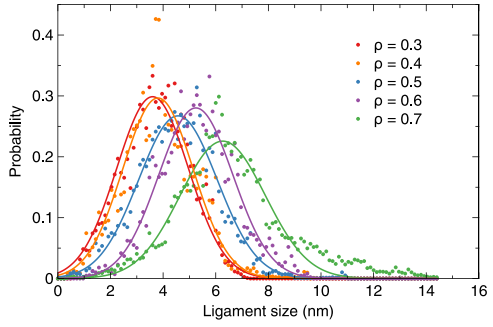

Fig. 2. Ligament size distributions for the initial structures with relative density ρ = 0.3, 0.4, 0.5, 0.6, and 0.7.

nm based on suitable images generated using the surface mesh tool of OVITO [58]. The algorithm implemented in AQUAMI as described by Stuckner et al. [57] first searches and identifies all ligaments and their medial axis. The shortest distance between positions along the ligament medial axis and ligament surface atoms is noted. Double of the distance gives the ligament diameter, or ligament size. The ligaments diameter measurement is made on several points in every ligament, generating thousands of measurements from each image. The ligament size distribution is displayed in Fig. 2 and indicates that the average ligament size varies from ~3.5 to ~6.2 nm.

2.2. Simulation details

After the generation of the bicontinuous nanoporous structure, the NPMG samples are relaxed at 50 K for 0.6 ns. The structure is then deformed under uniaxial tensile loading along the x-direction at a constant 3×10^8 s^{-1} strain rate. The temperature is maintained at 50 K and the stresses on the perpendicular directions to the loading, i.e., y and z directions, are kept at zero. The atomic-level stress and strain are calculated by LAMMPS [59] and OVITO, respectively.

All MD simulations used in the generation of the simulation model and to perform tensile loading tests are performed with LAMMPS. The interatomic potential proposed by Mendelev et al. [60] is used to describe interactions in the Cu-Zr binary alloy. All simulations use a constant integration timestep of 1 fs.

2.3. Genetic programming

To study the scaling laws of NPMGs, we employ GPSR to obtain symbolic expressions that can describe well the relation between properties, such as Eand UTS, and other variables, which in our case, are porosity and composition. The symbolic expressions are represented by binary expression trees [61]. There are two types of tree nodes. The first type is operation nodes, e.g., plus, minus, multiplication, division, and exponential. The second type is terminal nodes. Terminal nodes are variables and parameters. Among the first type, i.e., operation nodes, there are still two subtypes. The first one is binary operation nodes, e.g., plus and minus. The second type is unary operation nodes, e.g., exponential and sine. The binary operation nodes always have two child nodes, while the unary nodes only have a left child node. In this work, we chose to have unary operation nodes that are differentiable functions. This choice is made to allow efficient optimization of coefficients using the gradient-based Levenberg–Marquardt algorithm. In the literature, one can find implementations of the GPSR method also using nondifferentiable or discontinuous functions, such as the absolute function, $|x|$, step function, $\theta(x)$, or sign function, $\text{sign}(x)$ [53]. However, such functions prevent the use of highly efficient methods to obtain the optimized coefficients, and one has to resort to less efficient methods, e.g., by using the GP method itself.

Nodes of differet types and values are randomly chosen with assigned probabilities when creating a random expression. Fig. 3(a) illustrates an example of the binary tree representation of the symbolic expression given in Eq. (2)

$$2^{\frac{x}{y}}\left[\exp(x+y)+\frac{0.5}{\sin(x-y)}\right] \tag{2}$$

Each generation contains 80 symbolic expressions as its population. The parameters, if there are any, in each expression are fitted by the Levenberg–Marquardt algorithm. The efficiency of the GPSR method is enhanced with the use of the Levenberg–Marquardt algorithm. Without resorting to efficient methods, the GPSR would typically take ~50,000 generations to find solutions with similar accuracy as those obtained in this work, which is obtained with 800 generations. Using the efficient GPSR method, the required computational resources are modest, e.g., it takes about 40 minutes to reach a solution running the current GPSR implementation in an Intel Xeon E5-4660v4 processor. Expressions in each generation are sorted according to a score calculated based on the

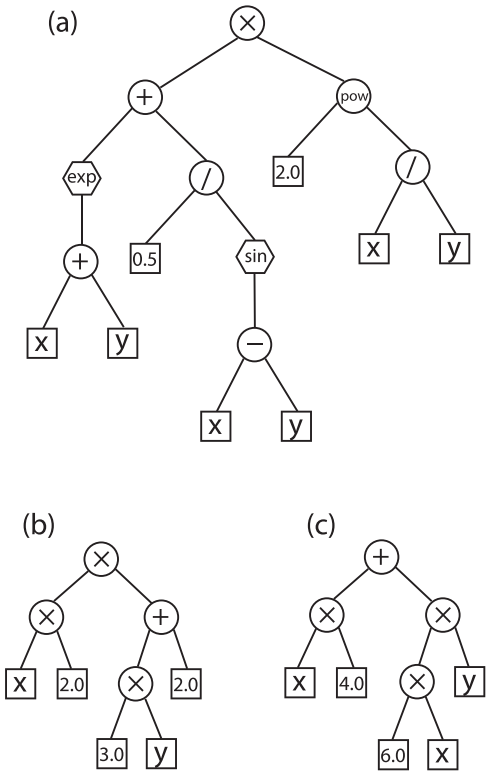

Fig. 3. Binary tree representations of symbolic expressions used in Genetic Programming (GP). (a)-(c) are examples of binary tree representations. (b) and (c) are two different binary trees of equivalent symbolic expressions. Circles and hexagons represent binary and unary operations, respectively. Squares represent terminals, i.e., numbers or variables.

mean square difference between predicted and true values, and a penalty value based on the number of nodes and coefficients. Evolutionary processes are then applied to each generation of symbolic expressions. The top 15% expressions in each generation are regarded as "elite" and are passed directly to the next generation. The remaining expressions in the next generation are obtained from the current generation of expressions following two evolutionary steps: crossover between two expressions, and possible mutation of the offspring expressions obtained from the crossover step. In the crossover step, two expression trees are chosen and each one of them is randomly cut at a certain node resulting in a branch. The branches are then attached to the other tree at the node where it was cut. In the mutation step, an offspring tree is cut at a certain node and a randomly generated subexpression is attached to that location. Similar to a natural selection process, expressions in the population with low scores have a higher chance to crossover and to have an offspring than those with high scores. Each offspring expression has a 20% chance to mutate, otherwise it is directly passed to the next generation. Crossover and mutation steps occur iteratively with the current generation of expressions until the complete set of 80 expressions of the next generation is obtained. After many generations of such evolutionary processes, the top expressions are expected to be able to predict well the scaling law of the mechanical behavior of NPMGs.

Several practical concerns need to be addressed in the GP algorithm. The first one is the generation of exceedingly long expressions, which may lead to overfitting. To alleviate this, we add a penalty to the number of nodes, i.e., the more nodes contained in the expression, the larger the penalty is. A restriction is also applied to the depth of the expressions trees, which is limited to seven. An additional concern is the existance of equivalent expressions, i.e., expressions with different binary tree representations yet the same value, e.g., Eqs. (3) and (4). The binary tree representations of Eqs. (3) and (4) are shown in Fig. 3(b) and (c).

$$2x(2+3y) \tag{3}$$

$$4x+6xy \tag{4}$$

The GP algorithm is implemented in Python with help of NumPy, Sympy, and SciPy libraries.To avoid equivalent expressions in the population, we take advantage of the capabilities of the Sympy library. Each generated expression is checked for any equivalence in the population. If an equivalent expression is found in the population the newly generated expression is eliminated.

3. Results

3.1. Geometrical and morphological features of bicontinuous NPMG

The initial NPMG structures for 5 different porosities, $\rho = 0.3$, 0.4, 0.5, 0.6 and 0.7, are shown in Fig. 1. The structures are self-similar to each other due to the level set method, i.e., the structures are generated from a common topology by scaling the porosity level. These bicontinuous structures consist of connected solid and porous phases. Fig. 1 also shows the normalized curvature distribution for the different initial NPMG structures. The two principal curvatures κ_1 and κ_2 are calculated by intially fitting bivariate surfaces represented by Eq. (5), considering the position of each surface atom and other surface atoms in its neighborhood, using the least square method

$$z(x,y) = ax^2 + by^2 + cxy + dx + ey + g \tag{5}$$

where $(x,\ y,\ z)$ are Cartesian coordinates and a, b, c, d, e, and g are parameters to be determined.

Once the parameters are found, the bivariate surface equation Eq. (5) can be reformulated into Eq. (6):

$$f(x,y,z) = x^2 + by^2 + cxy + dx + ey + g - z = 0 \tag{6}$$

which provides an implicit surface representation. The first- and second-order derivatives can be calculated as shown in Eq. (7):

$$f_x = d + 2ax + cy,\ \ f_y = e + 2by + cx,\ f_z = -1,\ f_{xx} = 2a,\ f_{yy} = 2b,\ f_{zz} = 0,\ f_{xy} = c,\ f_{xz} = 0,\ f_{yz} = 0 \tag{7}$$

The tangent planes and normal directions can be expressed with first-order derivatives of the function f given in Eq. (6). The tangent plane on $(x_0,\ y_0,\ z_0)$ other than (0, 0, 0) is given by $f_x(x_0,\ y_0,\ z_0)(x-x_0) + f_y(x_0,\ y_0,\ z_0)(y-y_0) + f_z(x_0,\ y_0,\ z_0)(z-z_0) = 0$, and the normal direction is given by $(f_x(x_0,\ y_0,\ z_0),\ f_y(x_0,\ y_0,\ z_0),\ f_z(x_0,\ y_0,\ z_0))$ on that point. The two principal curvatures can then be analytically calculated [62] based on the first- and second-order derivatives shown in Eqs. (8)–(11):

$$\kappa_H = (-1 \text{ or } 1) \times \frac{f_x^2(f_{yy}+f_{zz}) + f_y^2(f_{xx}+f_{zz}) + f_z^2(f_{xx}+f_{yy})}{2\cdot\left(f_x^2+f_y^2+f_z^2\right)^{3/2}} - \frac{f_x f_y f_{xy} + f_x f_z f_{xz} + f_y f_z f_{yz}}{\left(f_x^2+f_y^2+f_z^2\right)^{3/2}} \tag{8}$$

$$\kappa_K = 2\frac{f_x f_y(f_{xz}f_{yz} - f_{xy}f_{zz}) + f_x f_z(f_{xy}f_{yz} - f_{xz}f_{yy}) + f_y f_z(f_{xy}f_{xz} - f_{yz}f_{zz})}{\left(f_x^2+f_y^2+f_z^2\right)^2} + \frac{f_x^2\left(f_{yy}f_{zz} - f_{yz}^2\right) + f_y^2\left(f_{xx}f_{zz} - f_{xz}^2\right) + f_z^2\left(f_{xx}f_{yy} - f_{xy}^2\right)}{\left(f_x^2+f_y^2+f_z^2\right)^2} \tag{9}$$

$$\kappa_1 = \kappa_H - \sqrt{\left|\kappa_H^2 - \kappa_K\right|} \tag{10}$$

$$\kappa_2 = \kappa_H + \sqrt{\left|\kappa_H^2 - \kappa_K\right|} \tag{11}$$

It should be noted that to better fit the local surface, we rotate the Cartesian coordinates in order to align the z and normal directions. The sign of the mean curvature κ_H shown in Eq. (8) is 1 (-1) when the calculated surface normal is the same (opposite) as the actual normal, which can be determined following a procedure detailed elsewhere [18]. The curvatures are then normalized by the specific area. The curvature distribution for the $\rho = 0.5$ structure is symmetric with respect to the dashed lines in Fig. 1(c). Most of the surface at this porosity level is composed of saddle points. The surface has equal amounts of concave and convex areas indicated by the yellow and red rectangular regions, respectively. The remaining plots indicate that by increasing (decreasing) the relative density by 0.1, the surface displays more concave (convex) areas. As the relative density reaches $\rho = 0.7$ ($\rho = 0.3$) the structure contains mostly concave (convex) surface.

An important characteristic in bicontinuous NPMG is the ligament size distribution. Fig. 2 shows the calculated ligament size distributions for the 5 initial NPMG structures. In the calculation of the ligament sizes, we used 2 nm-thick slices randomly cut from the structures. These cross-sections are then used to evaluate the ligament size, which is done using the AQUAMI software [57]. For relative densities from $\rho = 0.3$ to $\rho = 0.7$ the estimated ligament size increases from 3.6 to 6.3 nm.

3.2. Mechanical properties of bicontinuous CuZr NPMG

We first focus on the mechanical properties of the samples with a Cu concentration of 0.64. The engineering stress-strain curves for $Cu_{64}Zr_{36}$ NPMG during tensile loading simulation for 7 samples, of which the relative density varies from 0.3 to 0.9, are represented in Fig. 4(a). The curves indicate a steady drop in both the stiffness and strength of the samples as the relative density decreases. For the samples with relative densities in the range from $\rho = 0.3$ to $\rho = 0.7$, the stress decreases gradually after reaching the apex (UTS) and the samples fail at around the strain value $\varepsilon = 0.4$. In contrast, the samples with relative densities $\rho = 0.8$ and $\rho = 0.9$ display a distinct behavior. The UTS is much higher (> 1.5 GPa) compared to the other 5 samples. In addition, the stress level drops sharply after reaching the UTS, indicating a different deformation mechanism. The stress-strain curves then stabilize at a certain level. This is a typical observation when simulating BMGs with periodic boundary conditions [63].

To investigate the effect of composition on the mechanical behavior of the CuZr NPMG samples, we consider the systems with initial dimensions 53.79 nm × 53.79 nm × 53.80 nm and vary the Cu concentration of the samples with different porosities. For each combination of porosity and composition a tensile loading simulation is performed to calculate the stress-strain relationship. Fig. 4(b) shows the engineering stress-strain curves obtained for samples with relative density $\rho = 0.5$ and Cu_xZr_{1-x} composition $x = 0.72$, 0.64, 0.50, 0.36, and 0.25. After performing the complete set of tensile loading simulations we evaluate the E and the UTS for each case. For the systems with relative density $\rho = 0.5$, it can be observed from the elastic regions that the E values increase with Cu concentration from 0.25 to 0.64. The exception is the $Cu_{72}Zr_{28}$ sample, which has a lower E value compared to the $Cu_{64}Zr_{36}$ sample. All samples display their UTS values at around 0.8 strain. The UTS values also increase with Cu concentration from 0.25 to 0.64. In contrast it drops in value from concentration 0.64 to 0.72. All bicontinuous NPMG samples with relative density $\rho = 0.5$ exhibit considerable plasticity compared to their BMG counterpart. Nevertheless, a clear change in plastic deformation mode and increase in ductility is observed in Fig. 4(b)

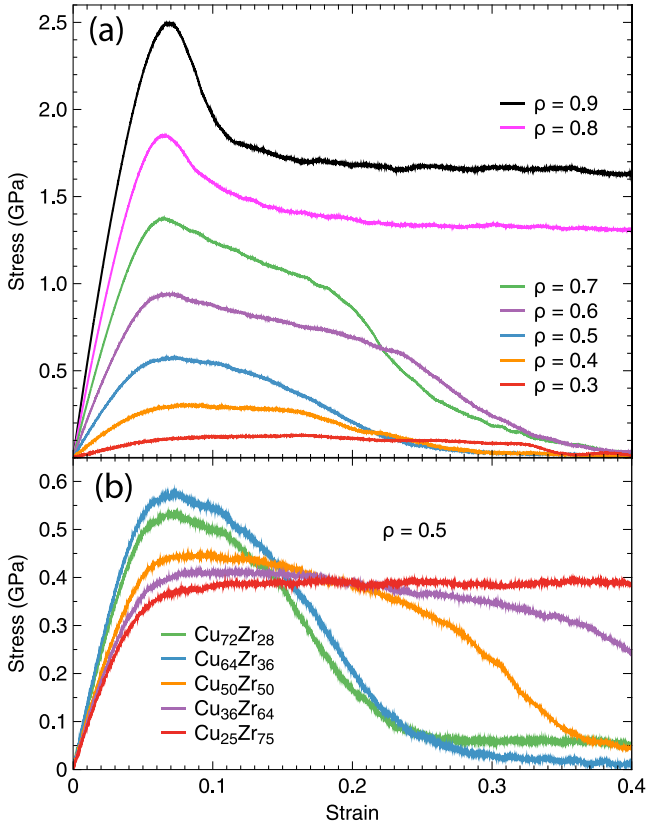

Fig. 4. Tensile loading engineering stress-strain relationships for the BNPMG samples investigated. (a) Stress-strain curves for $Cu_{64}Zr_{36}$ samples with different relative densities. (b) Stress-strain curves for samples with relative density ρ=0.5 and different compositions.

when Cu concentration drops from 0.64 to 0.25. In particular, the $Cu_{25}Zr_{75}$ system experiences a long plastic deformation regime displaying no signs of failure in the strain range displayed in Fig. 4(b). Nonetheless, the ductilities are similar for $Cu_{72}Zr_{28}$ and $Cu_{64}Zr_{36}$ samples. The complete set of E and UTS values, calculated from the mechanical behavior of the samples with different relative density–composition combinations is displayed in Fig. 5. It can be observed that for low relative density samples, the values of E and UTS are similar for different compositions. For relative densities different than $\rho = 0.5$, the plots also indicate that the values of E and UTS increase with Cu concentration from 0.25 to 0.64. The results indicate that the E and UTS values for $Cu_{64}Zr_{36}$ and $Cu_{72}Zr_{28}$ are similar at all relative densities considered.

For a system with given relative density and composition, we can expect an effect of the system size on the mechanical behavior, since the ligament size will scale with the size of the structure. To evaluate the possible size effects, additional simulations are performed. We construct multiple $Cu_{64}Zr_{36}$ samples with different system sizes to evaluate the dependence of the mechanical behavior on the ligament size while preserving the porosity and other morphological features. We consider system sizes in the range from 43.03 nm × 43.03 nm × 43.04 nm to 80.69 nm × 80.69 nm × 80.71 nm. We perform a series of tensile loading simulations considering all combinations of system size and relative density for the fixed $Cu_{64}Zr_{36}$ composition. Fig. 6 displays the values of E and UTS evaluated from the stress-strain curves obtained from the tensile loading simulations. It should be noted that for systems with small dimensions, low relative density, i.e., $\rho = 0.3$, cannot be achieved since the ligaments at those system are unstable and will collapse during the relaxation phase due to their exceedingly small

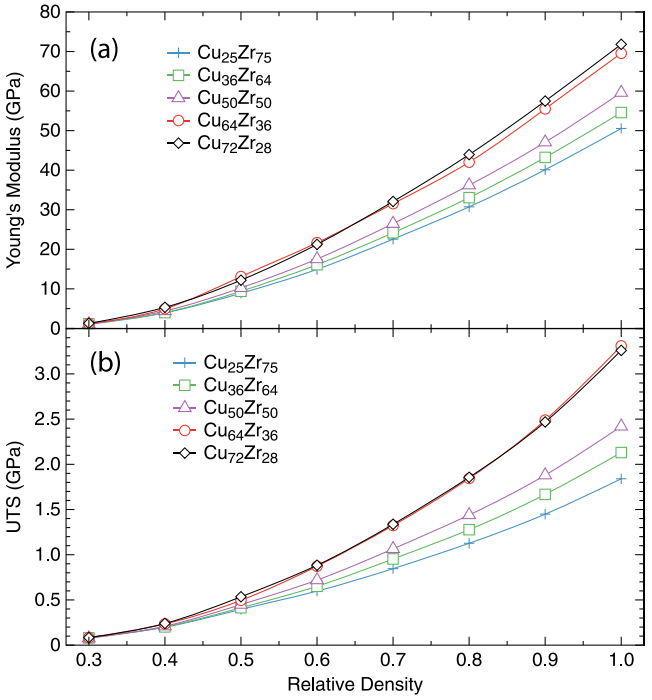

Fig. 5. Young's modulus and ultimate tensile strength (UTS) for samples with different compositions as a function of relative density.

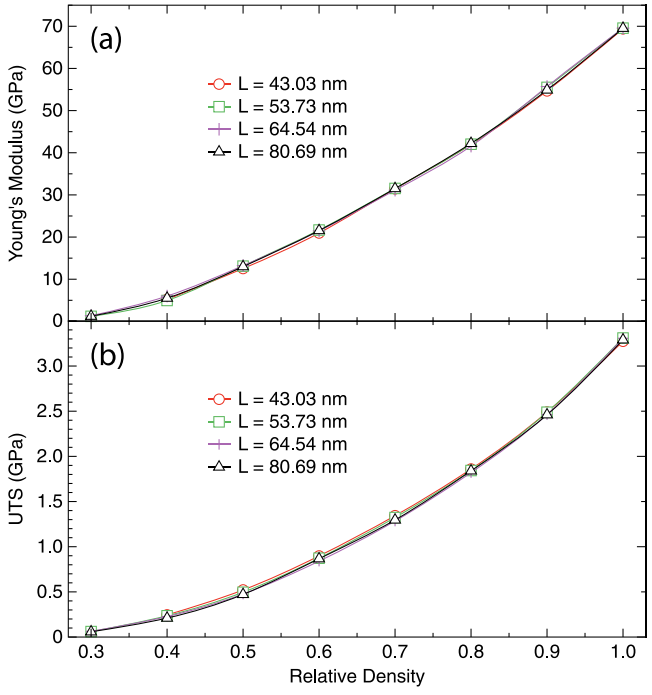

Fig. 6. Young's modulus and UTS for $Cu_{64}Zr_{36}$ samples with different system sizes as a function of relative density.

size, i.e., ligament sizes smaller than 2.8 nm. The results show that neither E nor UTS have a clear dependence on system size. The values for these two physical quantities are close for all system sizes and do not show any clear trend with increasing or decreasing system size while keeping the porosity and other morphological features constant.

3.3. Different deformation and failure modes for different relative densities

To better understand the change in overall elastic and plastic deformation modes for the samples with different relative density we need to quantify the local deformation developed in the structures during the tensile loading process. Fig. 7 shows the von Mises atomic local strain [64], for the representative samples with $\rho = 0.4$, 0.7, and 0.9 at an overall engineering strain of 0.36. One can observe a transition in deformation and failure modes from low to high relative density. The deformation of the samples with $\rho = 0.4$ and $\rho = 0.7$ is dominated by the deformation of ligaments in the structure. Those ligaments initially deform elastically and after exceeding their tensile strength develop necking and fail. The structures fail when massive failure of ligaments is triggered throughout the nanoporous structure as reported previously [18].

In contrast, the deformation in the sample with $\rho = 0.9$ occurs following a distinct mechanism. Different than the bicontinuous nanoporous samples with low relative density, the system with $\rho = 0.9$, which has closed pores, deforms and fails in a similar way as a typical BMG, i.e., by generation and evolution of a critical shear band. Nonetheless, different than in a BMG, where shear transformation zones (STZs) are generated homogeneously throughout the samples during tensile loading, in the sample with $\rho = 0.9$, the plastic deformation onset is dominated by STZs that are generated heterogeneously at the pores of the structure. The STZs evolve, generating an array of incipient shear bands in the nanoporous structure, which delocalize plastic deformation, resulting in smoother stress release from the UTS point compared to that displayed by a BMG sample. Eventually, one of the incipient shear bands becomes critical, and dominate the deformation of the structure as displayed in Fig. 7(c). The critical shear band traverses the structure at nearly 45 degrees with the loading direction in a similar way as a dominant shear band in a BMG. The change in deformation and failure mode observed from the analysis of the microstructures evolution is consistent with the stress-strain curves shown in Fig. 4(a).

3.4. Scaling laws uncovered by GPSR

It is instructive to understand how the mechanical properties of nanoporous materials scale with their structural features. In this work, GPSR is applied to find scaling relationships between materials properties: E and UTS (σ_u) and bicontinuous nanoporous variables: relative density (ρ) and Cu concentration (c). Each value of E and UTS corresponding to a combination of relative density and composition considered in this work is used as input data for the GPSR. The initial population of 80 expressions describing the relationships is generated randomly. After multiple GPSR runs, we obtain various expressions that are able to describe accurately the scaling relationships between mechanical properties and system variables. We display four such expressions developed for E and UTS in Tables 2 and 3, respectively. The corresponding root mean square error (RMSE) and normalized root mean square error (NRMSE) are calculated and displayed aside to quantify the accuracy of the expressions. The RMSE is calculated as $RMSE = \frac{\sqrt{\sum_{i=1}^{N}(x_i - \hat{x}_i)^2}}{N}$, where N is the number of data point, x_i the actual observations and $\hat{x}_i$ the estimated observations. The NRMSE is calculated as $NRMSE = \frac{RMSE}{\max(x_i) - \min(x_i)}$. The variety of equations and their diverse structures show the ability of the GP method at uncovering scaling laws with considerably independent forms. The top expressions in the two tables are considered the best scaling relations based on their accuracy and compactness. While they may not provide the ultimate lowest NRMSE values they have a

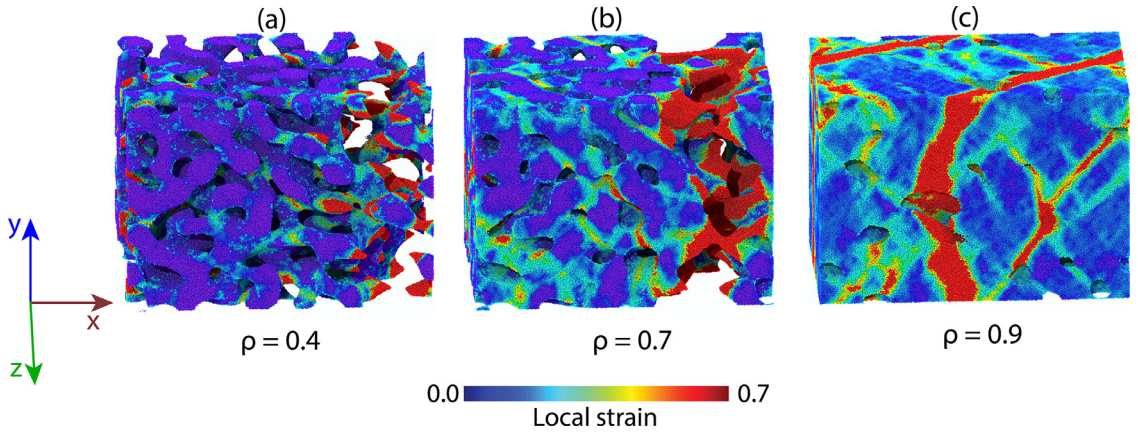

Fig. 7. Deformation and failure of $Cu_{64}Zr_{36}$ BNPMG samples with different relative densities. (a) and (b) samples fail by collective necking and failure of ligaments at ρ=0.4 and 0.7. (c) the sample with ρ=0.9 fails by shear banding.

Table 2
Scaling law for Young's modulus obtained by Genetic Programming.

Expression	RMSE (GPa)	NRMSE
$E = (c(2c+2)+2.5)(\rho^2(a_0+\rho)-1)$	1.57	0.022
$E = c\rho(a_0+\rho)(a_1+a_2c)$	1.24	0.037
$E = a_0 + c + \rho(a_1 + a_2e^{1.5c} + (a_3+a_4\rho)(a_5+c) + (a_6+a_7\rho^2)\sin(2c)) + \frac{2}{\rho}$	0.046	0.0038
$E = \rho(a_1+c)(a_2+a_3\rho) + (a_0+c)\log(\rho)$	0.53	0.012

Table 3
Scaling law for ultimate tensile strength obtained by Genetic Programming.

Expression	RMSE (GPa)	NRMSE
$\sigma_u = 2\rho(a_0+\rho)\times e^c$	0.12	0.49
$\sigma_u = (a_0\rho + c\rho)^{2.5}$	0.13	0.54
$\sigma_u = (a_0 + a_1c\rho^{\frac{a_2}{\rho}})(a_3+\rho)(c+\rho)$	0.11	0.46
$\sigma_u = \rho^2(2c+\rho)(a_0\rho^{a_1c+a_2\rho+a_3c^c} + a_4\rho + c)$	0.11	0.46

relatively simpler functional form and a lower number of coefficients.

It should be noted that in the GPSR implementation used in this work, we allow the algorithm to use coefficients, such as a_0, a_1, etc, that are fitted, and also constants, which are multiples of 0.5, such as 0.5, 1, 1.5, 2, etc, which are kept fixed. This allows the generation of expressions with common physical roots such as x^2, $\frac{x}{2}$, and $\frac{1}{\sqrt{(1-x)}}$. The comparison between the true values of E and UTS vs. those calculated from the first expressions shown in Table 2 and Table 3, are displayed in Figs. 8(a) and 8(b), respectively. The orange lines are used as reference and indicate perfect matching. Besides the values predicted with the equations developed with GPSR, Fig. 8 also shows values predicted with existing scaling laws [22]:

$$\frac{E}{E_b} = C_1\left(C_2\rho + \rho^2\right) \tag{12}$$

$$\sigma_u = \sigma_b C_3 \rho \tag{13}$$

where E is the Young's modulus of the foam, E_b and σ_b are the Young's modulus and the UTS of the bulk material, and C_1, C_2, and C_3 are constants to be determined. To obtain the values of E_b and σ_b used in Eqs. (11) and (12) additional tensile simulations are conducted for bulk $Cu_{25}Zr_{75}$, $Cu_{36}Zr_{64}$, $Cu_{50}Zr_{50}$, $Cu_{64}Zr_{36}$, and $Cu_{72}Zr_{28}$ MGs. The calculated Young's moduli are 38.36, 42.97, 47.35, 59.25, and 59.78 GPa, while the UTS are 1.84, 2.13, 2.42, 3.31, and 3.26 GPa, respectively.

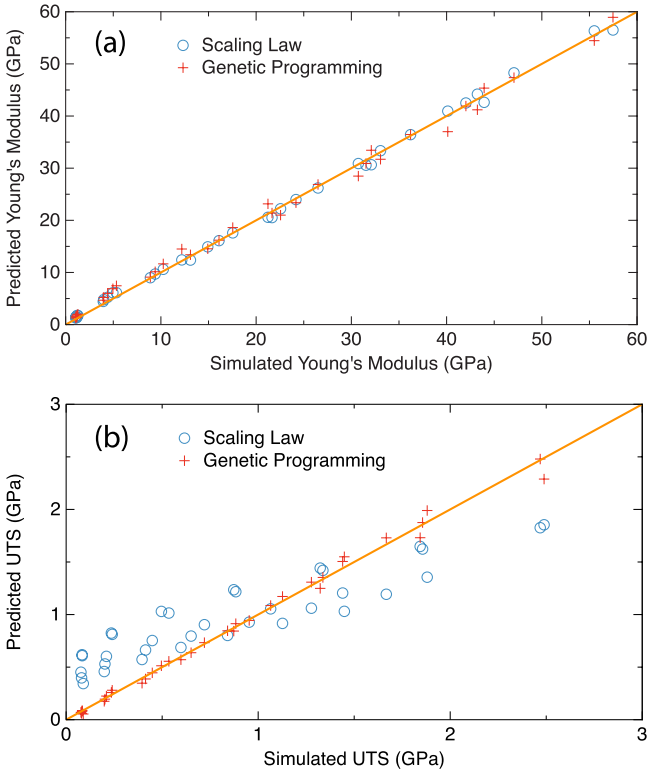

Fig. 8. Comparison between existing and GP derived scaling laws accuracy for the Young's modulus and UTS. (a) Predicted vs. simulated values for the Young's modulus and (b) UTS of samples with different relative densities and compositions. Perfect correlation is indicated by the reference orange line.

4. Discussions

4.1. System size effect on mechanical properties

As we change the system size, we found that the ligament size has negligible influence on the mechanical properties of bicontinu-

ous NPMG for all compositions when the porosity and other morphological features are kept fixed. Similar results have been found in the study of open cell porous $Cu_{50}Zr_{50}$ MG structures with $\rho = 0.5$ by Zhang et al. [23]. The results obtained from tensile loading simulations indicate the absence of dependence between E, the UTS, and the yield strength with the ligament size. Arguably, the absence of a clear effect of ligament size is linked to the absence of a change in deformation mode for the MG ligaments, which should occur at much larger critical ligament size as reported for MG nanopillars [65,66]. These results for MG samples contrast with the behavior predicted for crystalline nanoporous materials. Sun et al. [22] investigated the effect of ligament size on the mechanical properties of bicontinuous nanoporous gold and found negligible changes in the values of E and the yield strength. Nonetheless, they found that UTS values decrease with increasing ligament size. The small ligament size used in this work is expected to introduce significant surface energy and cause tension-compression asymmetry. Indeed, bicontinuous $Cu_{50}Zr_{50}$ MG studied by Zhang et al. [23] demonstrate different E and yield strength under tensile loading and compressive loading due to the large specific area. Both values are slightly higher under tensile loading. In addition, they suggest the tension-compression asymmetry is more significant in samples with larger porosity. The tension-compression asymmetry has also been reported in bicontinuous nanoporous gold samples [67,68].

4.2. Compositional effect on mechanical properties

Changes in composition typically lead to changes in the mechanical properties of materials. Our results indicate that the values of E and UTS increase with Cu concentration in the concentration range from $x = 0.25$ to 0.64. However, there is no clear changes in E and UTS values for concentrations beyond $x = 0.64$. Similar results have been found in the study of $Cu_{50}Zr_{50}$ and $Cu_{64}Zr_{36}$ BMGs [69], in which the $Cu_{50}Zr_{50}$ samples display lower values of E, yield stress, and UTS. In addition, higher Cu concentration significantly decrease the observed ductility of bicontinuous NPMGs, as observed in Fig. 4(b). This is in agreement with observed behavior in BMGs [69]. Previous investigations indicate that a higher fraction of atomic icosahedra motifs in the amorphous structure is linked to the higher strength and lower plasticity displayed by samples with higher Cu concentration [70,71]. Ward et al. [55] found that increase of Cu fraction in CuZr MG leads to increase of the fraction of Cu centered <0,0,12,0> full icosahedra (FI) until it reaches a maximum value at 0.7 Cu fraction, followed by a slight decrease with further increasing of Cu fraction. A higher density of icosahedra in the structure may lead to a network of interconnected icosahedra motifs. The network then behaves as a backbone that is resistant to stress-induced shear transformations during deformation. Imran et al. [72] studied the mechanical properties of $Cu_{25}Zr_{75}$, $Cu_{50}Zr_{50}$, and $Cu_{75}Zr_{25}$ MGs using indentation tests and conclude that samples with higher Cu concentrations display higher hardness and resistance force at the same load depth. Lee et al. [73] suggested that the connectivity of icosahedra network reaches 98% at 0.65 Cu fraction. Our results agree with these results and suggest that a high interconnectivity of icosahedra motifs is achieved at $x = 0.64$ [55,73]. To further support our analysis we estimate the fraction of interconnected icosahedra motifs of the samples used in this work. We first use Voronoi analysis to identify all atoms centered in FI atomic configurations. Then we apply coordination analysis to evaluate the spatial connectivity of these FI-centered atoms, i.e., by calculating the fraction of FI-centered atoms that have at least one bond with other FI-centered atoms. The results for each system with different Cu concentration are shown in Fig. 9. The fraction of FI-centered atoms increases sharply as Cu concentration increases from 0.25 to 0.64, followed by a slower pace of increase from 0.64 to 0.72 Cu concentration. On the other hand, the fraction of connected FI-centered atoms increases with the Cu concentration but saturates when the concentration exceeds 0.64. These results are in good agreement with those reported in the literature [55,73].

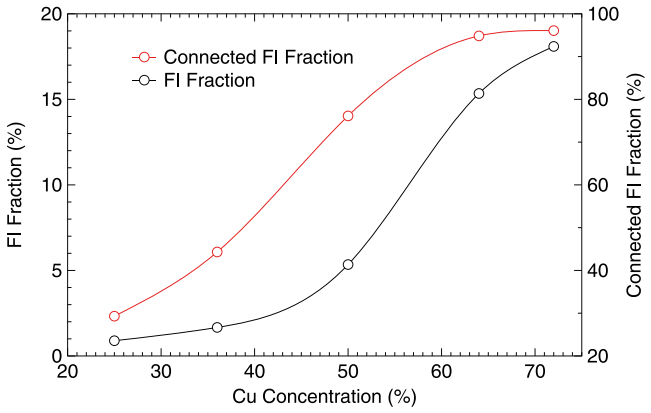

Fig. 9. Fraction of Full Icosahedra (FI) and connected FI as a function of Cu concentration in CuZr MG alloys. The lines are guides to the eye.

4.3. Existing scaling laws with relative density

It is interesting to compare the scaling laws obtained by the GP method with existing scaling laws. After thoroughly studying the mechanical properties of open-cell foams with micron or larger characteristic length scale, Gibbs and Ashby proposed the well-known scaling law [74] for Young's modulus based on Timoshenko beam theory shown in Eq. (14),

$$\frac{E}{E_b} = C_4\rho^2 \tag{14}$$

where C_4 is a coefficient to be determined. In the study of $Cu_{50}Zr_{50}$ bicontinuous NPMGs, Zhang et al. [19] found the relation between Young's modulus and relative density to be in good agreement with Eq. (14). From our results, after converting Eq. (14) to $E = E_bC_4\rho^2$ and finding the optimized value for C_4, considering all data, the obtained NRMSE value is about 5%.

While this accuracy is satisfactory, the scaling law proposed by Sun et al. [22] shown in Eq. (12) describes better how the mechanical properties scale with the relative density of bicontinuous NPMGs, i.e., NRMSE value of 1.2%. The proposed scaling law shown in Eq. (12) combines the effect of porosity [74] as well as the effect of ligaments deformation [75]. Sun et al. [22] used the cubic array unit cell model established by Gibbs and Ashby, which can account for the effect of ligaments [74]. The relative density ρ was assumed to be related to the ligament aspect ratio by $\rho \propto (d/l)^2$, where d and l are the ligament size and length, respectively. In addition, the normalized Young's modulus was also assumed to follow the same relationship $\frac{E}{E_b} \propto (d/l)^2$ [22].

Thus, $\frac{E}{E_b} \propto \rho$. The linear term was then added to Eq. (14) to obtain the proposed scaling law shown in Eq. (12). We use our data values for Young's modulus at different relative densities of MGs of different Cu concentrations and Eq. (12) to find the optimized values for the coefficients C_1 and C_2. The comparison between the simulation results and values obtained from Eq. (12) is shown in Fig. 8(a). We can see that this scaling law fits well the simulation data, displaying an NRMSE of 1.2%. The results show that the relationship provided in Eq. (12) further improves the agreement with simulation results from that obtained using Eq. (14).

Equation (12) was first proposed to describe the scaling relation for nanoporous gold [22]. Later it was also applied to study

nanoporous aluminum by Winter et al. [76], who also found good agreement.

In the original work of Sun et al. [22], Eq. (12) was tested considering relative densities in the range from 0.24 to 0.36, which is significantly narrower than those in our study. Our results show that Eq. (12) is also able to accurately predict the Young's modulus of bicontinuous CuZr NPMG considering a wide range of relative densities and also compositions. The fact that the same scaling law applies both for nanoporous crystalline metals and MGs reveals that their mechanical behavior is intrinsically similar, at least in the elastic region.

There are alternative scaling laws proposed in the literature for the mechanical behavior of nanoporous materials [21,77,78]. Pia et al. [77] studied the effective Young's modulus of nanoporous gold obtained from selective dissolution of Ag from a $Ag_{70}Au_{30}$ alloy, which was followed by thermal annealing. The ligament size of the nanoporous gold samples varied from 5 to 200 nm. They simplified the geometry of the nanoporous structure to that of a representative cubic unit cell and derived a scaling law of effective Young's modulus as a function of the shape factors of the ligaments, as well as the Young's modulus and Poisson ratio of bulk gold. Mangipudi et al. [21] investigated the stiffness of nanoporous gold considering three independent topologies: (i) 3D reconstruction from tomography of experimental nanoporous gold samples (ii) spinodal decomposed structure obtained from phase field simulations and (iii) a gyroid structure. They claimed that while the scaling law of Young's modulus for all topologies can be well described by Eq. (14), the pre-factor C_4 is linearly dependent on the genus of the particular nanoporous structure. Badwe et al. [78] studied the tensile properties of dealloyed nanoporous gold. The samples were thermally annealed to coarsen the ligaments. The Young's modulus was found to obey a power law. However, the calculated exponent was larger than that predicted by the Gibson-Ashby scaling law shown in Eq. (14). They further generalized the scaling law of Young's modulus proposing the law shown in Eq. (15)

$$\frac{E}{E_b} = C_1(C_2\rho + \rho^n) + C_3 \tag{15}$$

Among the scaling relationships proposed in the literature, the modified Gibbs and Ashby law provided in Eq. (12) is the most effective and succinct at describing relationships in a large range of relative densities.

As for the UTS, Sun et al. [22] proposed a linear relationship between the UTS and the relative density as shown in Eq. (13). It was demonstrated that Eq. (13) can describe well the scaling relation between porosity and UTS for bicontinuous nanoporous gold [22]. However, as illustrated in Fig. 8(b), the actual values of the UTS of CuZr bicontinuous NPMGs deviate considerably from the predictions of Eq. (13) with the value of the coefficient C_3 optimized to the data. The corresponding NRMSE is found to be 15%. Similar significant deviation in the predictions of UTS were also reported for $Cu_{50}Zr_{50}$ bicontinuous NPMGs [19]. This contrast in results between crystalline and amorphous samples implies that the scaling law for UTS of crystalline and amorphous materials is intrinsically distinct, which is expected since crystalline and amorphous metals deform plastically following different mechanisms.

4.4. Comparison of GPSR uncovered and existing scaling laws

The GPSR method is able to generate functional expressions with different forms that can accurately describe the scaling relationships between mechanical properties and system variables as shown in Table 2 and Table 3. For simplicity, only the top two expressions in Tables 2 and 3 are used in the calculation of the predictions shown in Figs. 8(a) and 8(b), respectively, as GP scaling laws for E and UTS. Those two expressions are able to describe well the values of E and UTS of bicontinuous nanoporous CuZr MGs, with NRMSE 2.2% and 5% for E and UTS, respectively. Compared to the predictions made with Eq. (13), which is the current scaling law for nanoporous gold, the predictions of the GP scaling law for UTS display a much better agreement with the simulation data. The corresponding NRMSE for the GP scaling law at 5% is much lower than that of the the current scaling law at 15%. The GP method is able to uncover the nonlinear relationship between UTS and relative density and assign appropriate expressions to it.

As for the predictions of the Young's modulus, the results indicate that both the current scaling law and the GP derived relationship predictions are in good agreement with the simulation data, with corresponding NRMSE of 1.2% and 2.2%, respectively. Even though the agreement is good in both cases, the GP scaling law is slightly less accurate than the predictions made with Eq. (12).

However, it should be noted that the scaling law derived with the GPSR method is universal and applicable to all compositions. In contrast, the current scaling law requires knowledge of the E_b value, which is used as an additional parameter to define the specific scaling law at each composition. Instead, the GP method is capable of uncovering the dependence of E_b on composition, which is typically not a simple increasing or decreasing relationship and incorporating it in the universal scaling law predicted. For instance, both E and UTS of bulk Cu_xZr_{1-x} MG increase from $x = 0.25$ to 0.64, and keep the same value in the range $0.64 < x < 0.72$.

While the accuracy of the predictions using the GP derived universal scaling law is good, it can be further improved if one allows more complicated expressions, with more fitting coefficients, to describe the nonlinear relationships, e.g., the third expression in Table 2. An important aspect of the GP method is that it is also able to retrieve the scaling law proposed based on physical insights, e.g., the second expression in Table 2 has the same form as the current scaling law shown in Eq. (12).

5. Conclusions

In this work, we have investigated the mechanical properties of bicontinuous nanoporous CuZr MGs with different relative densities, system sizes, and compositions during tensile loading using MD simulations. While the samples have self-similar structures, the relative density dictates the surface morphology and ligament size. We found that the system size of bicontinuous NPMG has little impact on the mechanical properties while the relative density and the Cu concentration have strong effects. A brittle-to-ductile transition occurs at relative density 0.7. Bicontinuous NPMGs with large relative density, e.g., 0.9, fail by developing a critical shear band, which is nucleated at large pores, while those with small relative density fail by progressive necking of ligaments. We employed the GP method to unravel universal scaling laws and compared their predictions with that of existing scaling laws. The scaling law based on Gibbs and Ashby's theory considering the effect of ligaments can be applied well to Young's modulus of bicontinuous nanoporous CuZr MGs. However, the existing linear scaling laws for UTS of nanoporous structure are not able to offer accurate predictions to the bicontinuous NPMGs studied in this work. Relationships uncovered by GPSR are able to find succinct expressions to describe accurately the dependence of mechanical properties on relative density and Cu concentration with physical insights.

Data availability

The data that support the findings of this study are available from the corresponding author on request.

Disclaimer

This report was prepared as an account of work sponsored by an agency of the United States Government. Neither the United States Government nor any agency thereof, nor any of their employees, makes any warranty, express or implied, or assumes any legal liability or responsibility for the accuracy, completeness, or usefulness of any information, apparatus, product, or process disclosed, or represents that its use would not infringe privately owned rights. Reference herein to any specific commercial product, process, or service by trade name, trademark, manufacturer, or otherwise does not necessarily constitute or imply its endorsement, recommendation, or favoring by the United States Government or any agency thereof. The views and opinions of authors expressed herein do not necessarily state or reflect those of the United States Government or any agency.

Declaration of competing interest

The authors declare that they have no known competing financial interests or personal relationships that could have appeared to influence the work reported in this paper.

Acknowledgements

This material is based upon work supported by the U.S. Department of Energy, Office of Science, Office of Basic Energy Sciences, under Award Number DE-SC0020295. Computation for the work described in this paper was supported by the University of Southern California Center for Advanced Research Computing (carc.usc.edu).

References

[1] M.F. Ashby, A.L. Greer, Metallic glasses as structural materials, Scr. Mater 54 (2006) 321–326, doi:10.1016/j.scriptamat.2005.09.051.
[2] Y. Bai, C. She, Atomic structure evolution in metallic glasses under cyclic deformation, Comput. Mater. Sci. 169 (2019) 109094, doi:10.1016/j.commatsci.2019.109094.
[3] J. Banhart, Manufacture, characterisation and application of cellular metals and metal foams, Prog. Mater. Sci. 46 (2001) 559–632, doi:10.1016/S0079-6425(00)00002-5.
[4] Y.C. Hu, Y.Z. Wang, R. Su, C.R. Cao, F. Li, C.W. Sun, Y. Yang, P.F. Guan, D.W. Ding, Z.L. Wang, W.H. Wang, A highly efficient and self-stabilizing metallic-glass catalyst for electrochemical hydrogen generation, Adv. Mater. 28 (2016) 10293–10297, doi:10.1002/adma.201603880.
[5] W.E. Brower, M.S. Matyjaszczyk, T.L. Pettit, G.V. Smith, Metallic glasses as novel catalysts, Nature 301 (1983) 497–499, doi:10.1038/301497a0.
[6] A. Inoue, A. Takeuchi, Recent development and application products of bulk glassy alloys☆, Acta Mater 59 (2011) 2243–2267, doi:10.1016/j.actamat.2010.11.027.
[7] J.Q. Wang, Y.H. Liu, M.W. Chen, G.Q. Xie, D.V. Louzguine-Luzgin, A. Inoue, J.H. Perepezko, Rapid degradation of Azo dye by Fe-based metallic glass powder, Adv. Funct. Mater. 22 (2012) 2567–2570, doi:10.1002/adfm.201103015.
[8] S. Hara, K. Sakaki, N. Itoh, H.M. Kimura, K. Asami, A. Inoue, An amorphous alloy membrane without noble metals for gaseous hydrogen separation, J. Memb. Sci. (2000), doi:10.1016/S0376-7388(99)00192-1.
[9] H.-J. Lin, M. He, S.-P. Pan, L. Gu, H.-W. Li, H. Wang, L.-Z. Ouyang, J.-W. Liu, T.-P. Ge, D.-P. Wang, W.-H. Wang, E. Akiba, M. Zhu, Towards easily tunable hydrogen storage via a hydrogen-induced glass-to-glass transition in Mg-based metallic glasses, Acta Mater 120 (2016) 68–74, doi:10.1016/j.actamat.2016.08.020.
[10] J. Schroers, C. Veazey, W.L. Johnson, Amorphous metallic foam, Appl. Phys. Lett. 82 (2003) 370–372, doi:10.1063/1.1537514.
[11] T. Wada, A. Inoue, A.L. Greer, Enhancement of room-temperature plasticity in a bulk metallic glass by finely dispersed porosity, Appl. Phys. Lett. 86 (2005) 251907, doi:10.1063/1.1953884.
[12] A.H. Brothers, D.C. Dunand, Syntactic bulk metallic glass foam, Appl. Phys. Lett. 84 (2004) 1108–1110, doi:10.1063/1.1646467.
[13] S. Tanaka, T. Kaneko, N. Asao, Y. Yamamoto, M. Chen, W. Zhang, A. Inoue, A nanostructured skeleton catalyst: suzuki-coupling with a reusable and sustainable nanoporous metallic glass Pd-catalyst, Chem. Commun. 47 (2011) 5985–5987, doi:10.1039/c1cc10710k.
[14] W. Jiao, P. Liu, H. Lin, W. Zhou, Z. Wang, T. Fujita, A. Hirata, H.W. Li, M. Chen, Tunable nanoporous metallic glasses fabricated by selective phase dissolution and passivation for ultrafast hydrogen uptake, Chem. Mater. 29 (2017) 4478–4483, doi:10.1021/acs.chemmater.7b01038.
[15] D. Şopu, C. Soyarslan, B. Sarac, S. Bargmann, M. Stoica, J. Eckert, Structure-property relationships in nanoporous metallic glasses, Acta Mater 106 (2016) 199–207, doi:10.1016/j.actamat.2015.12.026.
[16] H. Liu, Z. Chen, J. Mo, M. Wang, Y. Zhang, W. Yang, Brittle-to-ductile transition in monatomic Tantalum nanoporous metallic glass, J. Non. Cryst. Solids. 506 (2019) 6–13, doi:10.1016/j.jnoncrysol.2018.12.004.
[17] W.H. Lin, Y. Teng, Z.D. Sha, S.Y. Yuan, P.S. Branicio, Mechanical properties of nanoporous metallic glasses: insights from large-scale atomic simulations, Int. J. Plast. (2020) 102657, doi:10.1016/j.ijplas.2019.102657.
[18] C. Liu, S. Yuan, P.S. Branicio, Bicontinuous nanoporous design induced homogenization of strain localization in metallic glasses, Scr. Mater. 192 (2021) 67–72, doi:10.1016/j.scriptamat.2020.10.007.
[19] Y. Zhang, J. Li, Y. Hu, S. Ding, F. Du, R. Xia, Characterization of the deformation behaviors under uniaxial stress for bicontinuous nanoporous amorphous alloys, Phys. Chem. Chem. Phys. (2022) 1099–1112, doi:10.1039/d1cp04970d.
[20] Z. Zhang, C. Wang, P. Liu, K.M. Reddy, X. Wang, M. Chen, S. Song, Deformation behavior of a nanoporous metallic glass at room temperature, Int. J. Plast. 152 (2022) 103232, doi:10.1016/j.ijplas.2022.103232.
[21] K.R. Mangipudi, E. Epler, C.A. Volkert, Topology-dependent scaling laws for the stiffness and strength of nanoporous gold, Acta Mater 119 (2016) 115–122, doi:10.1016/j.actamat.2016.08.012.
[22] X.-Y. Sun, G.-K. Xu, X. Li, X.-Q. Feng, H. Gao, Mechanical properties and scaling laws of nanoporous gold, J. Appl. Phys. 113 (2013) 023505, doi:10.1063/1.4774246.
[23] Y. Zhang, Y. Xian, J. Li, S. Ding, S. Liu, R. Xia, Atomistic investigation on the mechanical properties of 3D nanoporous metallic glasses under uniaxial tension and compression, Mater. Today Commun. 27 (2021) 102460, doi:10.1016/j.mtcomm.2021.102460.
[24] J. Li, Y. Xian, H. Zhou, R. Wu, G. Hu, R. Xia, Microstructure-sensitive mechanical properties of nanoporous gold: a molecular dynamics study, Model. Simul. Mater. Sci. Eng. 26 (2018) 075003, doi:10.1088/1361-651X/aadb5d.
[25] J. Li, Y. Zhang, C. Tian, H. Zhou, G. Hu, R. Xia, Structurally ordered nanoporous Pt–Co alloys with enhanced mechanical behaviors in tension, Microporous Mesoporous Mater 295 (2020) 109955, doi:10.1016/j.micromeso.2019.109955.
[26] M. Schmidt, H. Lipson, Distilling free-form natural laws from experimental data, Science 324 (2009) 81–85 80-, doi:10.1126/science.1165893.
[27] R.R. Kline, Cybernetics, automata studies, and the dartmouth conference on artificial intelligence, IEEE Ann. Hist. Comput. 33 (2011) 5–16, doi:10.1109/MAHC.2010.44.
[28] W. Sha, Y. Guo, Q. Yuan, S. Tang, X. Zhang, S. Lu, X. Guo, Y.-C. Cao, S. Cheng, Artificial intelligence to power the future of materials science and engineering, Adv. Intell. Syst. 2 (2020) 1900143, doi:10.1002/aisy.201900143.
[29] A. Agrawal, A. Choudhary, Perspective: materials informatics and big data: Realization of the “fourth paradigm” of science in materials science, APL Mater 4 (2016) 053208, doi:10.1063/1.4946894.
[30] R.K. Vasudevan, K. Choudhary, A. Mehta, R. Smith, G. Kusne, F. Tavazza, L. Vlcek, M. Ziatdinov, S.V. Kalinin, J. Hattrick-Simpers, Materials science in the artificial intelligence age: High-throughput library generation, machine learning, and a pathway from correlations to the underpinning physics, MRS Commun 9 (2019) 821–838, doi:10.1557/mrc.2019.95.
[31] G. Panapitiya, G. Avendano-Franco, P. Ren, X. Wen, Y. Li, J.P. Lewis, Machine-learning prediction of CO Adsorption in Thiolated, Ag-Alloyed Au nanoclusters, J. Am. Chem. Soc. 140 (2018) 17508–17514, doi:10.1021/jacs.8b08800.
[32] N. Artrith, B. Hiller, J. Behler, Neural network potentials for metals and oxides - first applications to copper clusters at zinc oxide, Phys. Status Solidi Basic Res. 250 (2013) 1191–1203, doi:10.1002/pssb.201248370.
[33] H. Sahu, W. Rao, A. Troisi, H. Ma, Toward predicting efficiency of organic solar cells via machine learning and improved descriptors, Adv. Energy Mater. 8 (2018) 1801032, doi:10.1002/aenm.201801032.
[34] S. Lu, Q. Zhou, Y. Ouyang, Y. Guo, Q. Li, J. Wang, Accelerated discovery of stable lead-free hybrid organic-inorganic perovskites via machine learning, Nat. Commun. 9 (2018) 3405, doi:10.1038/s41467-018-05761-w.
[35] Z. Li, Q. Xu, Q. Sun, Z. Hou, W.-J. Yin, Thermodynamic stability landscape of halide double perovskites via high-throughput computing and machine learning, Adv. Funct. Mater. 29 (2019) 1807280, doi:10.1002/adfm.201807280.
[36] H. Salmenjoki, M.J. Alava, L. Laurson, Machine learning plastic deformation of crystals, Nat. Commun. 9 (2018) 5307, doi:10.1038/s41467-018-07737-2.
[37] E. Kim, K. Huang, A. Saunders, A. McCallum, G. Ceder, E. Olivetti, Materials synthesis insights from scientific literature via text extraction and machine learning, Chem. Mater. 29 (2017) 9436–9444, doi:10.1021/acs.chemmater.7b03500.
[38] N. Schneider, D.M. Lowe, R.A. Sayle, G.A. Landrum, Development of a novel fingerprint for chemical reactions and its application to large-scale reaction classification and similarity, J. Chem. Inf. Model. 55 (2015) 39–53, doi:10.1021/ci5006614.
[39] H. Zhang, S.K. Moon, T.H. Ngo, Hybrid machine learning method to determine the optimal operating process window in aerosol jet 3D printing, ACS Appl. Mater. Interfaces. 11 (2019) 17994–18003, doi:10.1021/acsami.9b02898.
[40] B. Lin, J.L. Hedrick, N.H. Park, R.M. Waymouth, Programmable high-throughput platform for the rapid and scalable synthesis of polyester and polycarbonate libraries, J. Am. Chem. Soc. 141 (2019) 8921–8927, doi:10.1021/jacs.9b02450.
[41] T.F. Gonzalez, Handbook of Approximation Algorithms and Metaheuristics, 2007, doi:10.1201/9781420010749.
[42] W. Li, K.G. Field, D. Morgan, Automated defect analysis in electron microscopic images, Npj Comput. Mater. 4 (2018) 36, doi:10.1038/s41524-018-0093-8.

[43] J.R. Koza, Genetic programming as a means for programming computers by natural selection, Stat. Comput. 4 (1994) 87–112, doi:10.1007/BF00175355.
[44] Y. Wang, N. Wagner, J.M. Rondinelli, Symbolic regression in materials science, MRS Commun 9 (2019) 793–805, doi:10.1557/mrc.2019.85.
[45] J.R. Koza, M.A. Keane, M.J. Streeter, W. Mydlowec, J. Yu, G. Lanza, Genetic Programming IV: Routine Human-Competitive Machine Intelligence, 2003.
[46] J. Zhong, L. Feng, W. Cai, Y.S. Ong, Multifactorial genetic programming for symbolic regression problems, IEEE Trans. Syst. Man, Cybern. Syst. 50 (2020) 4492–4505, doi:10.1109/TSMC.2018.2853719.
[47] K.N. Sastry, Genetic Algorithms and Genetic Programming for Multiscale Modeling: Applications in Materials Science and Chemistry and Advances in Scalability, 2007.
[48] G. Quaranta, W. Lacarbonara, S.F. Masri, A Review on Computational Intelligence for Identification of Nonlinear Dynamical Systems, Springer, Netherlands, 2020, doi:10.1007/s11071-019-05430-7.
[49] A. Prieto, B. Prieto, E.M. Ortigosa, E. Ros, F. Pelayo, J. Ortega, I. Rojas, Neural networks: an overview of early research, current frameworks and new challenges, Neurocomputing 214 (2016) 242–268, doi:10.1016/j.neucom.2016.06.014.
[50] F. Ghasemi, A. Mehridehnavi, A. Pérez-Garrido, H. Pérez-Sánchez, Neural network and deep-learning algorithms used in QSAR studies: merits and drawbacks, Drug Discov. Today. 23 (2018) 1784–1790, doi:10.1016/j.drudis.2018.06.016.
[51] P. Chopra, R.K. Sharma, M. Kumar, Prediction of compressive strength of concrete using artificial neural network and genetic programming, Adv. Mater. Sci. Eng. 2016 (2016) 1–10, doi:10.1155/2016/7648467.
[52] W. Cai, A. Pacheco-Vega, M. Sen, K.T. Yang, Heat transfer correlations by symbolic regression, Int. J. Heat Mass Transf. 49 (2006) 4352–4359, doi:10.1016/j.ijheatmasstransfer.2006.04.029.
[53] J. Im, C.B. Rizzo, F.P.J. de Barros, S.F. Masri, Application of genetic programming for model-free identification of nonlinear multi-physics systems, Nonlinear Dyn 104 (2021) 1781–1800, doi:10.1007/s11071-021-06335-0.
[54] S. Adibi, P.S. Branicio, S.P. Joshi, Suppression of shear banding and transition to necking and homogeneous flow in Nanoglass Nanopillars, Sci. Rep. 5 (2015) 15611, doi:10.1038/srep15611.
[55] L. Ward, D. Miracle, W. Windl, O.N. Senkov, K. Flores, Structural evolution and kinetics in Cu-Zr metallic liquids from molecular dynamics simulations, Phys. Rev. B. 88 (2013) 134205, doi:10.1103/PhysRevB.88.134205.
[56] C. Liu, P.S. Branicio, Efficient generation of non-cubic stochastic periodic bicontinuous nanoporous structures, Comput. Mater. Sci. 169 (2019) 109101, doi:10.1016/j.commatsci.2019.109101.
[57] J. Stuckner, K. Frei, I. McCue, M.J. Demkowicz, M. Murayama, AQUAMI: an open source Python package and GUI for the automatic quantitative analysis of morphologically complex multiphase materials, Comput. Mater. Sci. 139 (2017) 320–329, doi:10.1016/j.commatsci.2017.08.012.
[58] A. Stukowski, Visualization and analysis of atomistic simulation data with OVITO–the open visualization tool, Model. Simul. Mater. Sci. Eng. 18 (2010) 015012, doi:10.1088/0965-0393/18/1/015012.
[59] S. Plimpton, Fast parallel algorithms for short-range molecular dynamics, J. Comput. Phys. 117 (1995) 1–19, doi:10.1006/jcph.1995.1039.
[60] M.I. Mendelev, D.J. Sordelet, M.J. Kramer, Using atomistic computer simulations to analyze x-ray diffraction data from metallic glasses, J. Appl. Phys. 102 (2007) 043501, doi:10.1063/1.2769157.
[61] R.F.G.B.A. Forouzan, Data Structures: A Pseudocode Approach with C, 2nd ed., Cengage Learning, 2005.
[62] E. Albin, R. Knikker, S. Xin, C.O. Paschereit, Y. D'Angelo, Computational assessment of curvatures and principal directions of implicit surfaces from 3D scalar data, in: Lect. Notes Comput. Sci. (Including Subser. Lect. Notes Artif. Intell. Lect. Notes Bioinformatics), 2017, pp. 1–22, doi:10.1007/978-3-319-67885-6_1.
[63] K. Albe, Y. Ritter, D. Şopu, Enhancing the plasticity of metallic glasses: shear band formation, nanocomposites and nanoglasses investigated by molecular dynamics simulations, Mech. Mater. 67 (2013) 94–103, doi:10.1016/j.mechmat.2013.06.004.
[64] F. Shimizu, S. Ogata, J. Li, Theory of shear banding in metallic glasses and molecular dynamics calculations, Mater. Trans. 48 (2007) 2923–2927, doi:10.2320/matertrans.mj200769.
[65] X.L. Wang, F. Jiang, H. Hahn, J. Li, H. Gleiter, J. Sun, J.X. Fang, Plasticity of a scandium-based nanoglass, Scr. Mater. 98 (2015) 40–43, doi:10.1016/j.scriptamat.2014.11.010.
[66] S. Adibi, P.S. Branicio, R. Liontas, D.Z. Chen, J.R. Greer, D.J. Srolovitz, S.P. Joshi, Surface roughness imparts tensile ductility to nanoscale metallic glasses, Extrem. Mech. Lett. 5 (2015) 88–95, doi:10.1016/j.eml.2015.08.004.
[67] D. Farkas, A. Caro, E. Bringa, D. Crowson, Mechanical response of nanoporous gold, Acta Mater 61 (2013) 3249–3256, doi:10.1016/j.actamat.2013.02.013.
[68] M.H. Saffarini, G.Z. Voyiadjis, C.J. Ruestes, Temperature effect on nanoporous gold under uniaxial tension and compression, Comput. Mater. Sci. 200 (2021) 110766, doi:10.1016/j.commatsci.2021.110766.
[69] C.X. Peng, D. Şopu, Y. Cheng, K.K. Song, S.H. Wang, J. Eckert, L. Wang, Deformation behavior of designed dual-phase CuZr metallic glasses, Mater. Des. 168 (2019) 107662, doi:10.1016/j.matdes.2019.107662.
[70] M.H. Yang, J.H. Li, B.X. Liu, Proposed correlation of structure network inherited from producing techniques and deformation behavior for Ni-Ti-Mo metallic glasses via atomistic simulations, Sci. Rep. 6 (2016) 29722, doi:10.1038/srep29722.
[71] Z.W. Wu, M.Z. Li, W.H. Wang, K.X. Liu, Correlation between structural relaxation and connectivity of icosahedral clusters in CuZr metallic glass-forming liquids, Phys. Rev. B. 88 (2013) 054202, doi:10.1103/PhysRevB.88.054202.
[72] M. Imran, F. Hussain, M. Rashid, Y. Cai, S.A. Ahmad, Mechanical behavior of Cu—Zr bulk metallic glasses (BMGs): a molecular dynamics approach, Chinese Phys. B. 22 (2013) 096101, doi:10.1088/1674-1056/22/9/096101.
[73] M. Lee, C.M. Lee, K.R. Lee, E. Ma, J.C. Lee, Networked interpenetrating connections of icosahedra: effects on shear transformations in metallic glass, Acta Mater 59 (2011) 159–170, doi:10.1016/j.actamat.2010.09.020.
[74] L.J. Gibson, M.F. Ashby, Cellular Solids: Structure and properties, second edition, 2014, doi:10.1017/CBO9781139878326.
[75] G.F. Wang, X.Q. Feng, Surface effects on buckling of nanowires under uniaxial compression, Appl. Phys. Lett. 94 (2009) 2010–2013, doi:10.1063/1.3117505.
[76] N. Winter, M. Becton, L. Zhang, X. Wang, Failure mechanisms and scaling laws of nanoporous aluminum: a computational study, Adv. Eng. Mater. 18 (2016) 632–642, doi:10.1002/adem.201500315.
[77] G. Pia, M. Carta, F. Delogu, Nanoporous Au foams: variation of effective Young's modulus with ligament size, Scr. Mater. 144 (2018) 22–26, doi:10.1016/j.scriptamat.2017.09.038.
[78] N. Badwe, X. Chen, K. Sieradzki, Mechanical properties of nanoporous gold in tension, Acta Mater 129 (2017) 251–258, doi:10.1016/j.actamat.2017.02.040.